PROCEEDINGS OF THE ROYAL SOCIETY A

Proc. R. Soc. A (2008) **464**, 877–904
doi:10.1098/rspa.2007.0285
Published online 15 January 2008

Do magnetic micro-swimmers move like eukaryotic cells?

By Marcus Roper[1,*], Rémi Dreyfus[2], Jean Baudry[3], Marc Fermigier[4], Jérôme Bibette[3] and Howard A. Stone[1]

[1]*School of Engineering and Applied Sciences, Harvard University, Cambridge, MA 02138, USA*
[2]*Department of Physics, Center for Soft Matter Research, New York University, New York, NY 10003, USA*
[3]*Laboratoire Colloïdes et Matériaux Divisés, and* [4]*Laboratoire Physique et Mécanique des Milieux Hétérogènes, ESPCI, 75005 Paris, France*

Recent advances in micro-machining allow very small cargos, such as single red blood cells, to be moved by outfitting them with tails made of micrometre-sized paramagnetic particles yoked together by polymer bridges. When a time-varying magnetic field is applied to such a filament, it bends from side to side and propels itself through the fluid, dragging the load behind it. Here, experimental data and a mathematical model are presented showing the dependence of the swimming speed and direction of the magnetic micro-swimmer upon tunable parameters, such as the field strength and frequency and the filament length. The propulsion of the filament arises from the propagation of bending waves between free and tethered ends: here we show that this gives the micro-swimmer a gait that is intermediate between a eukaryotic cell and a waggled elastic rod. Finally, we extract from the model design principles for constructing the *fastest swimming micro-swimmer* by tuning experimental parameters.

Keywords: biofluid dynamics; micro-swimming; reciprocal theorem; continuum modelling

1. Introduction

Experimentation and modelling have shed light on some of the physical challenges that must be overcome by free-swimming flagellated micro-organisms. The swimming gaits of such micro-organisms can be split into two primitive strategies, respectively, those of bacteria and of free-swimming eukaryotic cells, though the two gaits share a common kinematical basis: the passing of a deformation wave along an extended force-generating limb or *flagellum* (Brennen & Winet 1977). Among bacteria like *Escherichia coli*, this deformation wave is propagated by the corkscrewing of bundles of co-rotating rigid helicoidal flagellar filaments (Berg & Anderson 1971), with each flagellum driven at its base by a rotatory engine. By contrast, the flagella of eukaryotic cells are internally driven by the oscillations of dynein motors connecting doublets of microtubules that

* Author for correspondence (mroper@deas.harvard.edu).

Received 25 October 2007
Accepted 18 December 2007

form a stiff backbone to the flagellum. In this case, the propulsive deformation consisting of a bending wave in a small sliding displacement of two microtubules is propagated along the flagellum (Brokaw 1972*b*).

Advances in micromanipulation have enabled direct measurement of the forces and torques generated in bacterial swimming and inference of swimming efficiency (Chattopadhyay *et al.* 2006), allowing theoretical models of locomotion (Lighthill 1976; Purcell 1997) to be tested. However, a lack of control over or measurement of the material properties of the axoneme bundle, or of the torques exerted by the distributed dynein motors, has prohibited the experimental tests of models for eukaryotic swimming (Machin 1963; Brokaw 1972*a*; Camalet & Jülicher 2000). Here, we report on the controlled actuation of a micrometre-sized magnetically activated artificial flagellum, which provides a direct experimental test of hydrodynamical models for internally forced flexible flagella.

After a brief description of the magnetic micro-swimmer, first introduced by Dreyfus *et al.* (2005), we present a mathematical model for the dynamics of the propulsive filament (Roper *et al.* 2006). A combination of numerical and asymptotic analyses of this model allows an effective comparison between the propulsion by a magnetically driven filament and a eukaryotic flagellum. Specifically, we ask whether the magnetic filament generates useable thrust for locomotion along the whole of its length, like a eukaryotic flagellum (Brennen & Winet 1977), or whether it instead resembles an elastic rod that is waggled at one end and generates useable thrust only with the short section of filament immediately adjacent to the point of application of the force (Wiggins *et al.* 1998; Lagomarsino *et al.* 2003; Lauga 2006).

In this study, we show that the dynamics of the magnetically actuated micro-swimmer are *intermediate* between the eukaryotic flagellum and the waggled rod. In the physically relevant limit of large magnetoelastic numbers (a dimensionless measure of the ratio of magnetic to elastic bending moments) and moderately high frequencies, the conformation of the filament is controlled by a balance between the viscous stresses and the action of the external torque. This balance should be contrasted with that governing the waggled rod, in which elastic stresses propagate the bending wave along the rod. Nonetheless, just as for the waggled rod, the magnetic micro-swimmer generates propulsive force along only a fraction of its length. Although the confinement length scale is set by the same physics that determines the propagation of bending waves in a flagellum, the swimming dynamics have much in common with a waggled rod swimmer, including exhibiting, in simulations and experiments, a large band of frequencies over which the swimming speed is almost independent of actuation frequency, as well as giving identical scalings for the dependence of swimming speed upon filament length. At the very highest frequencies, elastic stresses start to play a dominant role in the propagation of the propulsive bending wave, and the propulsive gait of the micro-swimmer approaches quantitatively the swimming gait of a waggled rod.

Finally, we use the physical insight thus obtained to tackle the practical question of determining the combination of material parameters and actuation conditions, which gives the fastest swimming micro-swimmer. It is shown that a nearly maximum swimming speed is achieved over a large plateau of values of the actuation frequency, but that swimming speed near the maximum is sensitive to the filament length.

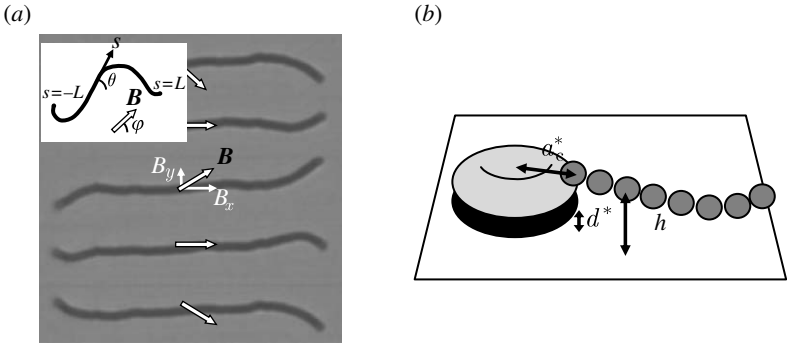

Figure 1. (*a*) Deformation of an isolated filament, consisting of 80 particles of 1 μm diameter, subjected to a uniform field $B_x = 9$ mT and transverse oscillating field with amplitude $B_a = 8$ mT and frequency $f = 20$ Hz. Images are taken at 12.5 ms intervals, and the instantaneous direction of the applied field $\boldsymbol{B}$ is denoted by black-outlined arrows. Annotations show the coordinate system adopted in §3. (*b*) Geometry of a cell-tethered magnetic micro-swimmer, including the lubrication layer thickness, d^*, filament to wall separation, h^*, and cell radius, a_c^*.

2. Experimental realization

Magnetic micro-swimmers are filaments made of superparamagnetic sub-micrometre diameter spheres, yoked together by polymer bridges. The protocols for constructing the filaments have been described in previous papers. Chains of superparamagnetic particles are self-assembled under a strong (approx. 30 mT) spatially homogeneous magnetic field. Polymer bridges are formed between the particles in each chain by the addition of short lengths of biotinylated double-stranded DNA to streptavidin-coated particles of micrometre diameter (Dreyfus *et al.* 2005; Koenig *et al.* 2005) or by adding polyacrylic acid to particles of diameter 750 nm (Goubault *et al.* 2003). Cell-tethered swimmers are constructed from DNA-linked filaments by adding human red blood cells that had been incubated in biotinylated PEG-NHS during assembly. The length and number of the polymer linkers in each bridge set the flexibility of the filament. The flexibility of the chain can be inferred from the examination of arched conformations that form when the filament is placed initially orthogonal to a strong uniform field (Goubault *et al.* 2003).

In order to generate motion in a controlled direction and with a controlled speed, two magnetic fields are employed. The filament is first aligned with a homogeneous static field B_x. In addition, a transverse sinusoidal field $B_y = B_a \sin(\omega t^*)$ with an adjustable frequency $f = \omega/2\pi$ is applied in the direction perpendicular to B_x. These two fields have comparable amplitude so that the resulting field $\boldsymbol{B} \equiv B_x \boldsymbol{e}_x + B_y \boldsymbol{e}_y$ oscillates around the x-axis (see figure 1*a* for a definition of the coordinate system). Since the particles are superparamagnetic, the induced dipole moments are always directed parallel to the instantaneous magnetic field, formed as the superposition of the applied field and the fields due to the dipole moments induced along the filament. Since the energy of any pair of dipoles is minimum when aligned, the particles in the filament experience torques that tend to align the filament with the instantaneous applied field, so

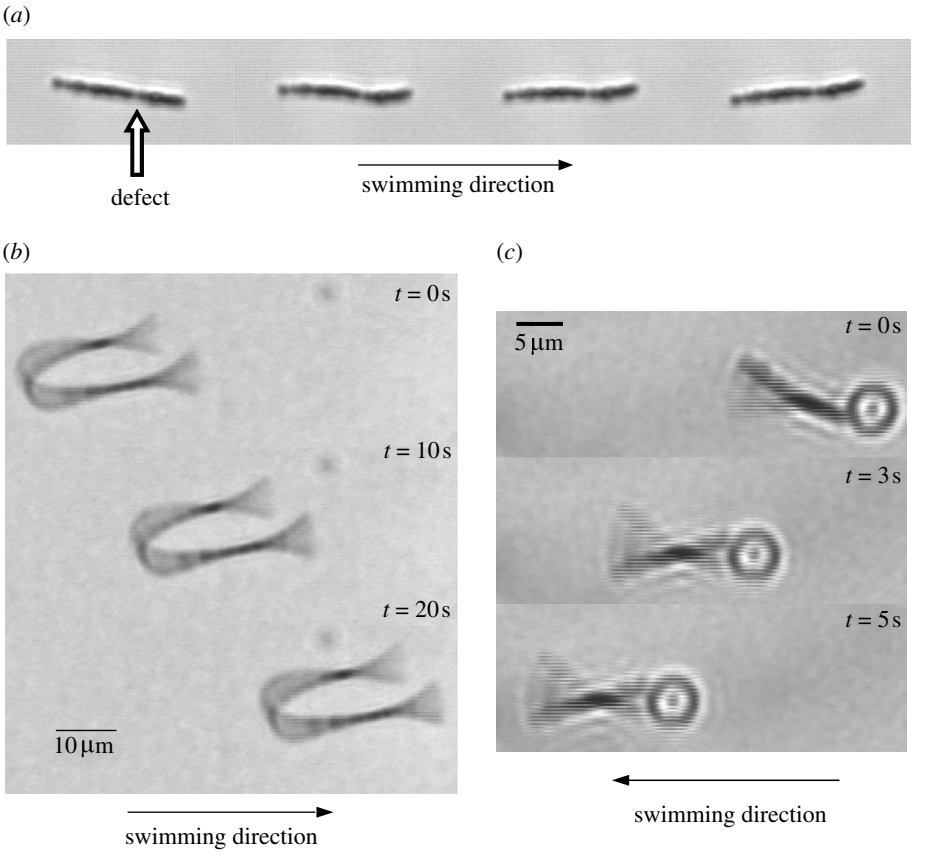

Figure 2. Three types of freely swimming micro-filaments. (*a*) Untethered filament showing a defect. The site of the defect, which is most likely caused by a low concentration of bound polymer, is marked with an arrow. (*b*) Hairpin swimmer. (*c*) Tethered swimmer. The micro-filament is attached to a red blood cell. Panel (*a*) has been adapted from Roper *et al.* (2006).

the free ends of an isolated filament will tend to follow the field direction. Viscous loading prevents the filament from rotating rigidly to follow the applied field, and so it bends with the phase of the filament away from the free ends lagging the phase of the free end. These are the necessary ingredients for the propagation of a bending wave away from the free end towards the centre of the filament (figure 1).

As the bending wave propagates along the filament, fluid is dragged in the direction of phase propagation. Since no external forces act upon the filament, there should be compensatory motion of the filament in the opposite direction (Taylor 1951). However, for an isolated defect-free swimmer, for which the deformation modes are symmetric about the centre line (figure 1*a*), the propulsive viscous forces exerted by the two 'arms' cancel exactly.

Some modification is therefore needed to break the symmetry of the forces generated. Three methods for breaking this symmetry—effectively eliminating either the leftward- or rightward-propagating components of the bending wave—are shown in figure 2.

The two arms of an isolated filament may differ in respect of the following.

(i) *Material properties*. Variations of bending stiffness arise from variation in the number and quality of DNA bridges between adjacent particles. In one such extreme case, the defects of very small bending stiffness may be seen, allowing large curvatures to be developed at specific points along the filament. Filaments constructed by this method always swim with the shorter arm forward (Roper *et al.* 2006), as shown in figure 2*a*.

(ii) *Geometry*. Sufficiently long filaments do not always align with a static applied field, but may form folded structures (Goubault *et al.* 2003; Cēbers 2005; Roper *et al.* 2006). These structures are not stable, except when the arch deforms plastically, presumably by a reorganization of the DNA linkages at the arch. The two arms of such a structure point in the same direction so that the viscous forces generated by the deforming arms sum, and the filament swims with its free ends foremost (Cēbers 2005), as shown in figure 2*b*.

(iii) *Kinematics*. If one arm is attached to a high drag object such as a red blood cell, it is prevented from following the applied field. The increase in viscous loading on the tethered arm of the filament suppresses the bending wave, and the filament swims with its free arm forward (Dreyfus *et al.* 2005), as shown in figure 2*c*.

3. A model for the dynamics of the driven filament

We review a previously derived continuum model for the conformational changes of the filament, in which the magnetic and elastic properties of the filament are represented on a coarse-grained level by the equations of a driven elastica, and hydrodynamic drag treated with resistive force theory (Cēbers 2003; Roper *et al.* 2006). The interactions between the dipole moments induced in the beads and the external field appear as a body torque $\boldsymbol{\tau}^*$ distributed along the length of the filament. We have assumed that the deformation of the filament is confined to a single plane. Such an approximation is certainly acceptable for an untethered filament, since the magnetic torque upon the filament acts in a direction normal to the plane of the crossed magnetic fields. However, for cell-tethered swimmers, the cells are seen to roll from side to side as they track the end of the filament, which tends to pull the filament out of the plane of the crossed fields. The rolling is particularly pronounced when the filament is not large when compared with the cell, and probably accounts for the discrepancy between the theoretical and experimental swimming speeds for short filaments (Dreyfus *et al.* 2005).

Denote the tangential (tensile) and normal stress resultants along a filament by $\mathit{\Lambda}^*$ and N^* respectively, the torque resultant by M^* and the tangential and normal components of the velocity of the elastica by v_{s}^* and v_{n}^*. A balance of internal to external stresses along the filament allows us to relate the stress resultants to the filament velocity

$$\frac{\partial}{\partial s^*}(\mathit{\Lambda}^*\boldsymbol{s} + N^*\boldsymbol{n}) = \zeta_{\parallel} v_{\mathrm{s}}^*\boldsymbol{s} + \zeta_{\perp} v_{\mathrm{n}}^*\boldsymbol{n}, \tag{3.1}$$

where $\zeta_{\parallel}$ and $\zeta_{\perp}$ are, respectively, the parallel and perpendicular resistive force coefficients (Lighthill 1976; Yu *et al.* 2006) and the parameter $-L < s^* < L$ measures distance along the centre line of the elastica. A balance of moments upon an infinitesimal element of filament gives

$$\frac{\partial M^*}{\partial s} + \tau^* = -N^*. \tag{3.2}$$

The conformation of the filament is described by a single angle variable $\theta(s, t)$ defined as the angle between the tangent to the elastica $\boldsymbol{s}$ and the x-axis (the static field direction) as shown in figure 1. The polymer bridges between particles resist any relative rotation of the particle, and on the scale of our model we may characterize this elastic response using a bending stiffness K_{b} relating the torque resultant within the filament to the strain: $M^* = K_{\mathrm{b}}\partial\theta/\partial s^*$ (Goubault *et al.* 2003). Cast in a dimensionless form[1] the inextensibility constraint and force and torque balances give us equations for the filament tension and evolution of the angle variable

$$\alpha\frac{\partial^2 \Lambda}{\partial s^2} = \left(\frac{\partial\theta}{\partial s}\right)^2 \Lambda + \left((\alpha+1)\frac{\partial\theta}{\partial s}\frac{\partial}{\partial s} + \alpha\frac{\partial^2\theta}{\partial s^2}\right)N, \tag{3.3a}$$

$$\Omega\frac{\partial\theta}{\partial t} = \frac{\partial^2\theta}{\partial s^2}\Lambda + (\alpha+1)\frac{\partial\theta}{\partial s}\frac{\partial\Lambda}{\partial s} - \left(\alpha\left(\frac{\partial\theta}{\partial s}\right)^2 - \frac{\partial^2}{\partial s^2}\right)N, \tag{3.3b}$$

$$N = -\frac{\partial^2\theta}{\partial s^2} - M_n S(\theta, t; b_0), \tag{3.3c}$$

$$S(\theta, t; b_0) \equiv b_0 \sin t \cos 2\theta - \frac{1}{2}\left(1 - b_0^2 \sin^2 t\right)\sin 2\theta. \tag{3.3d}$$

We review the four dimensionless parameters that feature in these governing equations.

(i) The drag anisotropy factor $\alpha \equiv \zeta_{\perp}/\zeta_{\parallel}$ is equal to the ratio of normal to tangential drag coefficients.
(ii) The oscillatory field strength $b_0 \equiv B_a/B_x$.
(iii) The magnetoelastic number

$$M_n \equiv \frac{\pi(aB_xL)^2}{6\mu_0 K_b}\frac{\chi^2}{(1-\chi/6)(1+\chi/12)} \tag{3.4}$$

(in which we have assumed that the particles have some isotropic susceptibility, χ (Dreyfus *et al.* 2005), and write a for the particle radius and μ_0 for the free space permeability) encodes the relative strength of magnetic to elastic stresses. When static magnetic fields are applied to the filament, any curvature developed by the filament tends to condense into features with $O(M_n^{-1/2})L$ length scale, such as the arches of long-lived hairpin conformations that filaments may adopt if initially orthogonal to the applied field (Goubault *et al.* 2003; Roper *et al.* 2006).

[1] Denoting the bending stiffness of the filament by K_{b} and its length by $2L$, we define dimensionless variables: $N^* = K_{\mathrm{b}}N/L^2$; $\Lambda^* = K_{\mathrm{b}}\Lambda/L^2$; $s^* = Ls$; and $t^* = t/\omega$.

(iv) The dimensionless frequency

$$\Omega \equiv \frac{\zeta_\perp \omega L^4}{K_\mathrm{b}}, \tag{3.5}$$

gives a measure of the relative importance of viscous and elastic forces. If one end of a long filament were clamped to a wall, and the free end waggled by a localized force, then a length $L/\Omega^{1/4}$ of filament would be mobilized by the forcing (Wiggins *et al.* 1998).

In equations (3.3*a*)–(3.3*d*), the function S contains all of the angle and time variation of the magnetically induced torque: $\tau = M_n S$.

In our experiments, the magnetic micro-swimmers are slightly denser than the surrounding fluid and, at the time that measurements of swimming speed are made, have sedimented to the floor of the capillary tube. The drag upon the filament is enhanced by its close proximity to the floor. Denoting the separation of the filament from the floor of the tube by h, we estimate the size of the drag enhancement using the formula (Happel & Brenner 1973)

$$\zeta = \frac{\zeta^\infty}{1 - \frac{3\zeta^\infty L}{32\pi\eta h}}, \tag{3.6}$$

where ζ may stand for either the resistive force coefficients $\zeta_\perp$ or $\zeta_\parallel$, and ζ^∞ denotes their far-field values, which we may, without too severe error, take equal to the values determined theoretically for a rigid spheroid (Cox 1970; Meunier 1994)

$$\zeta_\perp^\infty = \frac{4\pi\eta}{\log(L/a) + 1/2}, \qquad \zeta_\parallel^\infty = \frac{2\pi\eta}{\log(L/a) - 1/2}. \tag{3.7}$$

In order to model the three classes of micro-swimmer described above, it is necessary to devise continuum representations for the two different filament end conditions that may be realized in experiment. The first condition corresponds to the end of the filament being left free, for which appropriate boundary conditions are

$$N = 0, \quad \Lambda = 0 \quad \text{and} \quad \frac{\partial\theta}{\partial s} = 0. \tag{3.8}$$

Save for our discussion of swimming direction in §6*c*, which may be illuminated by studying the dynamics of an untethered filament, we will henceforth limit our analysis to swimmers of the third class, in which one end (which we identify as the boundary $s=1$) is left free and the other ($s=-1$) is tethered to a red blood cell. The cell does not come into contact with the floor of the tube, but appears (from indirect inference of the drag that it experiences) to sit on a thin (approx. 100 nm) cushion of fluid that we presume to be maintained by some combination of electrostatic, steric or elastohydrodynamic forces (Dreyfus *et al.* 2005). Although the swimming filament may be imaged only from above, out-of-plane rotation of the cell allows us to measure the cell thickness in some cases and, in line with these measurements, we treat the cell throughout as pill shaped with radius equal to its height. We set the separation of the filament from the wall to be equal to the radius of the cell (i.e. $h = a_\mathrm{c}^*$) in (3.6). For a typical micro-swimmer, the cell radius is $a_\mathrm{c}^* = 3.5$ μm and the half-length of the filament is $L=15$ μm. We write $a_\mathrm{c} = a_\mathrm{c}^*/L$ for the dimensionless cell radius. Figure 1*b* shows the three length scales that must be introduced in order to describe the geometry of a cell-tethered swimmer.

We extend our resistive force model to include the drag upon the 'cargo', by introducing an additional pair of drag coefficients: D_{t}^{*} for translation and D_{r}^{*} for rotation in the plane of the applied magnetic fields, so that the (dimensional) force required to propel the cell without rotation at speed U^{*} is given by $F^{*}=D_{\mathrm{t}}^{*}U^{*}$, and the torque required to rotate the cell at some angular velocity ω_{c}^{*} by $T^{*}=D_{\mathrm{r}}^{*}\omega_{\mathrm{c}}^{*}$. These drag coefficients have dimensionless counterparts $D_{\mathrm{t}}=D_{\mathrm{t}}^{*}/\zeta_{\perp}L$ and $D_{\mathrm{r}}=D_{\mathrm{r}}^{*}/\zeta_{\perp}L^{3}$. Although we enjoy little experimental control over the manner in which the filament is attached to the cell, it is typically seen that the point of attachment lies on the outer perimeter of the cell and that there is no relative motion of filament and cell (i.e. the filament may be considered to be 'clamped' to the cell). Balances of normal and tangential forces and torques upon the cell then yield

$$\left.\begin{aligned} N=D_{\mathrm{t}}\Omega U_{\mathrm{n}}\equiv D_{\mathrm{t}}\Omega\left(v_{\mathrm{n}}-a_{\mathrm{c}}\frac{\partial\theta}{\partial t}\right), \qquad \Lambda=D_{\mathrm{t}}\Omega U_{\mathrm{s}}\equiv D_{\mathrm{t}}\Omega v_{\mathrm{s}}, \\ \text{and} \\ D_{\mathrm{r}}\Omega\frac{\partial\theta}{\partial t}=Na_{\mathrm{c}}+\frac{\partial\theta}{\partial s}. \end{aligned}\right\} \tag{3.9}$$

We estimate the drag coefficients for the cargo by assuming that the drag upon the red blood cell is dominated by the fluid resistance within the lubrication layer (giving $D_{\mathrm{t}}^{*}=\eta\pi a_{\mathrm{c}}^{*2}/d^{*}$ and $D_{\mathrm{r}}^{*}=2\eta\pi a_{\mathrm{c}}^{4}/3d^{*}$ for a gap of thickness d^{*}). For a typical cell-tethered micro-swimmer in water, the dimensionless drag coefficients and filament geometrical parameters take values

$$\alpha=1.83, \quad a_{\mathrm{c}}=0.23, \quad D_{\mathrm{t}}=4.68 \quad \text{and} \quad D_{\mathrm{r}}=0.13. \tag{3.10}$$

The accuracy of this system of equations as a model for the dynamics of a magnetic micro-swimmer was shown in previous work (Dreyfus *et al.* 2005). Fidelity was the weakest for short filaments, for which the neglect of hydrodynamic interactions between the filament and its cargo is inadmissible and rotation of the cell/filament system about a horizontal axis becomes significant.

(*a*) *Inferring swimming speed from stroke kinematics*

The computed conformations $\theta(s,t)$ of the micro-swimmer can be simply related to its swimming speed by finding the resistance tensor of a rigid filament in each of the conformations $\theta(s,t)$. Our treatment parallels previous studies of non-filamentary deformable swimmers (Stone & Samuel 1996; Yariv 2006). Specifically, suppose that at some instant both the conformation of the swimmer $\theta(s,t)$ and the stress resultants Λ, N, and moment resultant M are all known. Now consider a reference swimmer, with identical conformation but different set of stress and moment resultants $\hat{\Lambda}$, $\hat{N}$ and $\hat{M}$, and velocities $\hat{v}_{\mathrm{s}}$, $\hat{v}_{\mathrm{n}}$ and $\partial\hat{\theta}/\partial t$. Then, by appealing to the force balance relation (3.1) we obtain

$$[v_{\mathrm{n}}\hat{N}+v_{\mathrm{s}}\hat{\Lambda}-\hat{v}_{\mathrm{n}}N-\hat{v}_{\mathrm{s}}\Lambda]_{s=-1}^{1}=\int_{-1}^{1}\left[(\hat{N}\boldsymbol{n}+\hat{\Lambda}\boldsymbol{s})\cdot\frac{\mathrm{d}\boldsymbol{v}}{\mathrm{d}s}-(N\boldsymbol{n}+\Lambda\boldsymbol{s})\cdot\frac{\mathrm{d}\hat{\boldsymbol{v}}}{\mathrm{d}s}\right]\mathrm{d}s. \tag{3.11}$$

Use of inextensibility and of the Serret and Frenet formulae gives $\mathrm{d}v/\mathrm{d}s = (\partial\theta/\partial t)\boldsymbol{n}$ for a forced filament, so the r.h.s. of (3.11) may be simplified to $\int_{-1}^{1}(\hat{N}(\partial\theta/\partial t) - N(\partial\hat{\theta}/\partial t))\mathrm{d}s$.

Next, take for a reference state a rigid filament/cell system with the same instantaneous conformation as our filament. Suppose that this reference filament is propelled by a force $\hat{F}$ applied at the centre of the red blood cell and directed along the x-axis, and that a point torque $\hat{T}$ is applied at the centre of the cell in order to prevent the filament from rotating. Then, the reference filament will translate without rotation (with velocity $\hat{\boldsymbol{v}} = \hat{U}$) so that (3.11) simplifies to

$$\hat{F}\,\boldsymbol{U}\cdot\hat{\boldsymbol{x}} = a_{\mathrm{c}}\hat{N}\frac{\partial\theta}{\partial t}\bigg|_{s=-1} + \int_{-1}^{1}\hat{N}\frac{\partial\theta}{\partial t}\mathrm{d}s. \tag{3.12}$$

In order to compute the swimming speed $\boldsymbol{U}\cdot\hat{\boldsymbol{x}}$ of the filament, the stress resultant $\hat{N}$ must be known for the reference state of a forced rigid filament. One route to determining this function is to integrate directly the force balance equations (3.1). If we represent the orthogonal components of the stress resultants and centre line velocity as the real and imaginary parts of complex fields, $\hat{\mathit{\Lambda}} + \mathrm{i}\hat{N}$ and $\hat{U} = \hat{U}_x + \mathrm{i}\hat{U}_y$, respectively, then the force balance equations can be assembled into a simple form

$$\frac{\partial}{\partial s}[\mathrm{e}^{\mathrm{i}\theta}(\hat{\mathit{\Lambda}} + \mathrm{i}\hat{N})] = \frac{\mathit{\Omega}}{2\alpha}[(\alpha+1)\hat{U} - (\alpha-1)\bar{\hat{U}}\mathrm{e}^{2\mathrm{i}\theta}], \tag{3.13}$$

where an overbar has been used to denote the complex conjugate of the rigid filament velocity. This equation may be integrated, and on application of the boundary conditions at the red blood cell it becomes

$$\hat{F} = \mathit{\Omega}D_{\mathrm{t}}\hat{U} + \frac{\mathit{\Omega}}{2\alpha}\left(2(\alpha+1)\hat{U} - (\alpha-1)\bar{\hat{U}}\int_{-1}^{1}\mathrm{e}^{2\mathrm{i}\theta(s,t)}\mathrm{d}s\right). \tag{3.14}$$

This linear equation may be inverted to obtain the rigid-body velocity $\hat{U}$ of the filament in response to the (arbitrary) applied force $\hat{F}$. Integration of (3.13) then gives us the stress resultant everywhere along the rigidified filament ($\hat{N}(s,t)$), which may be substituted into (3.12) to obtain the swimming speed.

By using a co-moving system of coordinates to resolve body deformation in response to the applied torques and then (3.12) to back out the velocity of the body afterwards, we separate the tasks of solving for the shape of the filament $\theta(s,t)$ and the speed of translation of the swimmer. Moreover, application of the formula (3.12) will allow us to solve only for the leading-order shape of the filament in several physically distinguished limits. These limits correspond to forcing scenarios for which further simplification of (3.12) is possible: in which the motion of the filament can be decomposed into a small deformation on top of a (possibly large) rigid-body motion, so that $\theta(s,t) \equiv \psi_0(t) + \epsilon\theta_1(s,t)$, where $\epsilon \ll 1$. In this case, we may approximate $\mathrm{e}^{2\mathrm{i}\theta} \approx \mathrm{e}^{2\mathrm{i}\psi_0}(1 + 2\mathrm{i}\epsilon\theta_1)$. The two cases $\psi_0 \equiv 0$ and $|\psi_0| \gg O(\epsilon)$ must be treated separately.

(*b*) *No rigid-body motion:* $\psi_0 \equiv 0$

By inverting (3.14) we find $\hat{U}_x = \hat{U}_{0x} + O(\epsilon^2)$ and $\hat{U}_y = \epsilon\hat{U}_{0y} + O(\epsilon^2)$ where

$$\hat{U}_{0x} = \frac{\hat{F}}{\mathit{\Omega}(D_{\mathrm{t}} + 2/\alpha)} \quad \text{and} \quad \hat{U}_{1y} = \frac{(\alpha-1)L_1^{(1)}(-1,t)\hat{F}}{\mathit{\Omega}\alpha(D_{\mathrm{t}}+2)(D_{\mathrm{t}}+2/\alpha)}. \tag{3.15}$$

Here we have defined a series of functions $L_1^{(1)}(s,t)=\int_s^1 \theta_1(s',t)\mathrm{d}s'$, $L_1^{(n+1)}(s,t)=\int_s^1 L_1^{(n)}(s',t)\mathrm{d}s'$. Hence, from (3.13)

$$\hat{N}(s,t)=\frac{\epsilon\hat{F}}{D_t\alpha+2}\left[(\alpha-1)L_1^{(1)}(s,t)+(1-s)\theta_1(s,t)-\frac{(\alpha-1)(1-s)}{D_t+2}L_1^{(1)}(-1,t)\right], \tag{3.16}$$

plus $O(\epsilon^2)$ terms. Substituting for $\hat{N}$ in (3.11), we then arrive at an equation for the time-averaged swimming speed of the filament

$$\langle \boldsymbol{U}\cdot\hat{\boldsymbol{x}}\rangle = \frac{\epsilon^2(\alpha-1)}{D_\mathrm{t}\alpha+2}\left\langle \frac{L_1^{(1)}(-1,t)}{D_\mathrm{t}+2}\frac{\partial}{\partial t}\left(L_1^{(2)}(-1,t)+D_\mathrm{t}a_\mathrm{c}\theta_1(-1,t)\right)\right.$$
$$\left.+\int_{-1}^{1}L_1^{(1)}(s',t)\frac{\partial\theta_1(s',t)}{\partial t}\,\mathrm{d}s'\right\rangle+O(\epsilon^4), \tag{3.17}$$

where we use single angled brackets as a shorthand for taking the time average. The time-averaged swimming speed is quadratic in the amplitude of the filament deformation, ϵ.

(*c*) *Large rigid-body motion:* $|\psi_0|\gg\epsilon$

In the case where the rigid-body component of the motion is large, by inverting (3.14) we determine the velocity of the rigid filament up to terms of $O(\epsilon^2)$

$$\hat{U}_x=\frac{\hat{F}}{\Delta}\left[D_\mathrm{t}+\frac{(\alpha+1)}{\alpha}+\frac{(\alpha-1)}{\alpha}\cos 2\psi_0-\frac{\epsilon(\alpha-1)}{\alpha}L_1^{(1)}(-1,t)\sin 2\psi_0\right], \tag{3.18a}$$

$$\hat{U}_y=\frac{\hat{F}(\alpha-1)}{\alpha\Delta}\left[\sin 2\psi_0+\epsilon L_1^{(1)}(-1,t)\cos 2\psi_0\right], \tag{3.18b}$$

in which $\Delta\equiv(D_\mathrm{t}+2)(D_\mathrm{t}+2/\alpha)$. Thus from (3.13)

$$\hat{N}(s,t)=\frac{\hat{F}}{D_\mathrm{t}+2}(1-s)\sin\psi_0+\frac{\epsilon\hat{F}}{D_\mathrm{t}\alpha+2}\left[(\alpha-1)L_1^{(1)}(s,t)+(1-s)\theta_1(s,t)\right.$$
$$\left.-\frac{(\alpha-1)(1-s)}{D_t+2}L_1^{(1)}(-1,t)\right]\cos\psi_0. \tag{3.19}$$

By substituting in (3.12) we obtain the time-averaged swimming speed of the filament

$$\langle \boldsymbol{U}\cdot\hat{\boldsymbol{x}}\rangle=\frac{\epsilon(\alpha-1)}{\alpha\Delta}\left\langle\left[2(D_\mathrm{t}+1)\left(L_1^{(2)}(-1,t)-L_1^{(1)}(-1,t)\right)\right.\right.$$
$$\left.\left.+a_\mathrm{c}D_\mathrm{t}\left(L_1^{(1)}(-1,t)-\theta_1(-1,t)\right)\right]\cos\psi_0\frac{\mathrm{d}\psi_0}{\mathrm{d}t}\right\rangle+O(\epsilon^2). \tag{3.20}$$

The time-averaged swimming speed is linear in the amplitude of the non-rigid-body component of the filament motion.

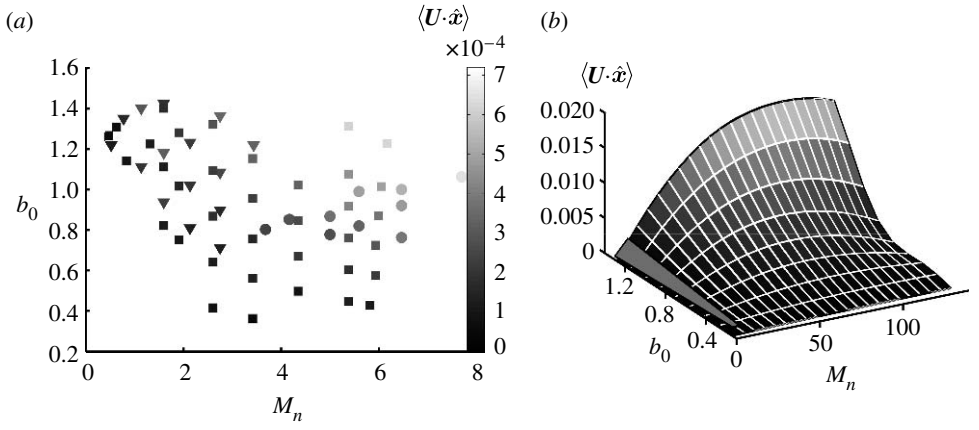

Figure 3. Evolution of the dimensionless swimming speed as a function of the ratio of field strengths, b_0, and magnetoelastic number, M_n (3.4). (*a*) Experimentally observed swimming speed, compiled from three swimmers: inverted triangles, $L=10.0$ μm; squares, $L=11.8$ μm; circles, $L=13.1$ μm. All three swimmers are actuated at $f=50$ Hz. The dimensionless swimming speed is given by the shading of data points, according to the colour key on the right side of the figure. (*b*) Predicted swimming speed (simulation) for an enlarged range of magnetoelastic numbers, for a single swimmer ($L=11.8$ μm, $\Omega=87.7$). The shaded trapezium on the lower left of the plot marks the parameter range assayed experimentally in (*a*).

4. Speed of swimming

For a single cell-tethered swimmer, we measure experimentally the swimming speed while cycling through the amplitudes of the two components of the applied magnetic field. This approach permits us to vary the two dimensionless parameters b_0 and M_n, while conserving the dimensionless frequency of actuation Ω. The variation of swimming speed with these two parameters is shown in figure 3*a*. It is impossible to continue the measurements above a field ratio $b_0 \approx 1.4$; above this critical field ratio, the direction of swimming ceases to align with the steady component of the field, a phenomenon that has already been observed in numerical simulations (Gauger & Stark 2006). We will explain the mechanism underpinning the reorientation of the swimmer in §6*c*. Up to this cut-off, the absolute swimming speed is seen to increase monotonically as either M_n or b_0 is increased. We contend that this monotonicity would not persist if the experimental assay had been continued up to much larger magnetic fields.

In figure 3*b*, we show the swimming velocity determined by numerical simulation of the equations (3.3*a*)–(3.3*d*) and covering an augmented range in M_n, i.e. longer filaments and stronger magnetic fields. In our simulations, we discretize the equations by replacing s-derivatives by centred differences, and simultaneously solve the nonlinear equations for the tensions and the fictive angles (used to enforce the boundary conditions) and advance the filament shape using the Matlab implicit DAE solver ode15 s. The non-monotonic dependence of swimming speed upon M_n over this enlarged range (which would have been seen in experiment if, for example, both field strengths and filament lengths had been doubled) is analogous to the non-monotonic variation with actuation frequency of the force exerted by a locally actuated elastic filament (Wiggins *et al.* 1998), an observation that will be explored in §5.

Although the coupled nonlinear partial differential equations for the evolution of the angle variable and tension within the filament must in general be solved numerically, quantitatively accurate expressions for how varying the material parameters (i)–(iv) affects the maximum swimming speed may be arrived at by analytical study of several distinguished limits. We focus upon developing asymptotic formulae for the swimming speed in the case where the magnetoelastic number, M_n, is either very large or very small.

(*a*) *Asymptotic results: small M_n (short stiff filaments)*

If $M_n \ll 1$, then non-monotonic variation of swimming speed with frequency is seen only if the motion is driven by a slowly time-varying magnetic field: $\Omega = M_n \Omega_1$. In this case, relaxation of field-induced curvature is only very weakly damped, and the motion of the filament reduces to a rigid-body rotation upon which an $O(M_n)$ deformation may be superimposed: $\theta \sim \psi_0(t) + M_n \theta_1(s,t) + O(M_n^2)$. We can determine both the form of the rigid-body rotation and the small deformation components of the motion by balancing viscous and elastic stress terms in (3.3*b*) to arrive at an equation

$$\Omega_1 \frac{\mathrm{d}\psi_0}{\mathrm{d}t} = -\frac{\partial^2 N_1}{\partial s^2}, \quad \text{with} \quad N_1 = -\frac{\partial^2 \theta_1}{\partial s^2} + \frac{1}{2}\left(1 + b_0^2 \sin^2 t\right)\sin(2(\phi - \psi_0)), \tag{4.1}$$

upon which we impose boundary conditions

$$N_1 = 0 \quad \text{and} \quad \frac{\partial \theta_1}{\partial s} = 0 \quad \text{at} \quad s = 1 \tag{4.2}$$

and

$$a_\mathrm{c} D_\mathrm{t} \Omega_1 \frac{\mathrm{d}\psi_0}{\mathrm{d}t} = D_\mathrm{t} \frac{\partial N_1}{\partial s} - N_1 \quad \text{and} \quad D_\mathrm{r} \Omega_1 \frac{\mathrm{d}\psi_0}{\mathrm{d}t} = a_\mathrm{c} N_1 + \frac{\partial \theta_1}{\partial s} \quad \text{at} \quad s = -1. \tag{4.3}$$

Recall here that ϕ is the time-varying angle of the applied field $\tan\phi = B_y/B_x$. On integrating up (4.1) and applying these boundary conditions, we obtain the deformation up to a $O(M_n)$ rigid-body motion, which we denote by $\psi_1(t)$

$$\begin{aligned}\theta_1(s,t) = \Omega_1 \frac{\mathrm{d}\psi_0}{\mathrm{d}t} \Bigg(&-\frac{(1-s)^4}{24} + \frac{((2+a_\mathrm{c})D_\mathrm{t} + 2)(1-s)^3}{6(D_\mathrm{t}+2)} \\ &- \frac{\left(4 + D_\mathrm{t}(8 + 12a_\mathrm{c} + 6a_\mathrm{c}^2 + 3D_\mathrm{r}) + 6D_\mathrm{r}\right)(1-s)^2}{12(D_\mathrm{t}+2)} \Bigg) + \psi_1. \end{aligned} \tag{4.4}$$

In order to balance torques on the red blood cell (and thereby satisfy the second of the boundary conditions (4.3)), it is necessary that

$$\Omega_1 \frac{\mathrm{d}\psi_0}{\mathrm{d}t} = \frac{6(D_\mathrm{t}+2)\left(1 + b_0^2 \sin^2 t\right)\sin(2(\phi - \psi_0))}{4 + D_\mathrm{t}(8 + 12a_\mathrm{c} + 6a_\mathrm{c}^2 + 3D_\mathrm{r}) + 6D_\mathrm{r}}. \tag{4.5}$$

If we wish to solve for the $O(M_n)$ rigid-body component of the filament motion, $\psi_1(t)$, it would be necessary to extend our expansion for the filament shape up to terms of $O(M_n^2)$. However, this is not necessary for a computation of the

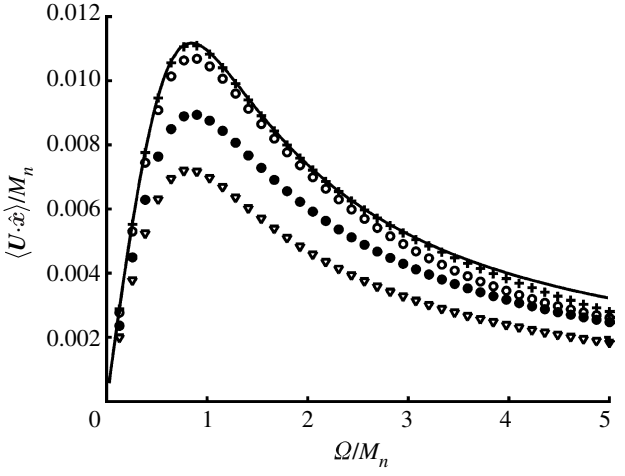

Figure 4. Comparison of the asymptotic expression for the swimming speed at small M_n (solid curve) with the numerical solution of equations (3.3*a*)–(3.3*d*). Crosses, $M_n=0.01$; open circles, 0.1; filled circles, 0.5; inverted filled triangles, 1.0. For all of the curves $b_0=1.0$ and the other geometrical parameters have been assigned the typical experimental values given in (3.10).

swimming speed, since the rigid-body part of the motion is reversible and will not contribute to the translation of the swimmer over a complete cycle of a magnetic field, as can be confirmed by substituting in the expression for the swimming speed (3.20). The expression for the swimming speed obtained by substituting for θ_1 and $\mathrm{d}\psi_0/\mathrm{d}t$ in (3.20) is cumbersome and we do not reproduce it here. We compare the asymptotic expression for the swimming speed with a numerical integration of the full time evolution and inextensibility equations (3.3*a*)–(3.3*d*) in figure 4. The parameters D_r, D_t, α and a_c cannot be continuously controlled in experiment, and we fix them at typical values given in (3.10).

The swimming dynamics change as the frequency of actuation is increased. If the actuation frequency Ω is increased to some $O(1)$ value, the oscillation of the filament is very severely damped and the rigid-body component disappears. Instead the filament oscillates with some $O(M_n)$ amplitude around a mean orientation, which may be either aligned to or else orthogonal to the steady component of the applied field. We write $\theta \sim (\pi/2-)M_n\theta_1(s,t)+O(M_n^2)$ to represent both of the possible gaits, and solve for the conformation of the filament in appendix A*a*. We will discuss how the mean orientation is selected in §6*c*.

(*b*) *Asymptotic results: large M_n and small b_0 (long filaments strongly actuated)*

In the limit $M_n \gg 1$, non-monotonicity of the swimming speed is seen only at high actuation frequencies $\Omega \sim O(M_n)$. To resolve this non-monotonicity analytically, we rescale $\Omega = M_n\Omega_1$. In order for the governing equations to be tractable, we make an additional simplification that $b_0 \ll 1$ and seek to compute the swimming speed up to terms of $O(b_0^2)$. In principle, the computation can be continued to incorporate higher order terms in b_0, although in practice leading-order expressions are known to suffice for many classes of swimmer

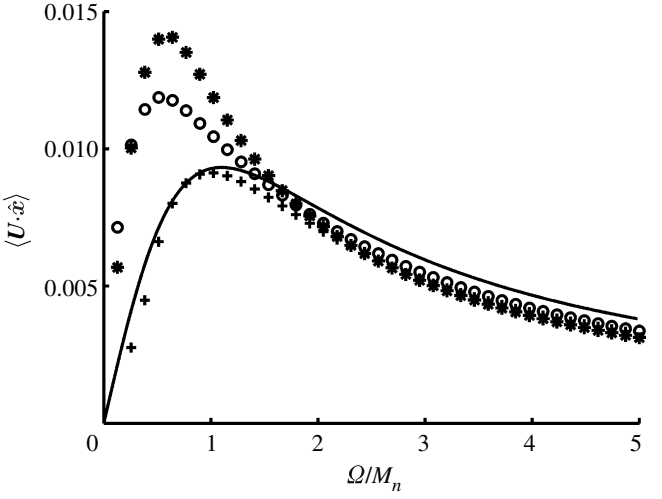

Figure 5. Comparison of the asymptotic expression for swimming in the $M_n \to \infty$ limit (solid curve) with numerical simulation of the fully nonlinear equations of motion (3.3*a*)–(3.3*d*). Asterisks, $M_n = 10$; open circles, 50; crosses, 100 to the $M_n \to \infty$ asymptotic limit (solid curve) (4.13). $b_0 = 1$, and other material parameters are assigned typical values from experiment (3.10).

(Yu *et al.* (2006) and see figure 5). If we write $\theta = b_0\theta_1 + O(b_0^2)$, then linearization of (3.3*a*)–(3.3*d*) produces

$$M_n \Omega_1 \frac{\partial \theta_1}{\partial t} = -\frac{\partial^4 \theta_1}{\partial s^4} + M_n \frac{\partial^2 \theta_1}{\partial s^2}. \tag{4.6}$$

The normal stress balance features a hyperdiffusive term representing elastic (bending) stress, while a second diffusive term represents the tension-like effect of the magnetic dipole–dipole interactions, which acts to straighten the filament. The tendency of these torques to align the entire filament with the direction of the external field is felt only through the boundary conditions upon the filament. Unlike elastohydrodynamic models of driven flagellae (Wiggins *et al.* 1998; Lagomarsino *et al.* 2003), the dominant balance of stresses upon the filament does not feature bending torques, except near the ends of the filament, but rather is between these magnetic torques, and the viscous resistance to deformation of the filament. In order to highlight contrasts with these elastohydrodynamic models, we define a parameter analogous to the dimensionless wavenumber that appears in these problems, $S_{\mathrm{p1}} = \Omega_1^{1/4}$ (Lagomarsino *et al.* 2003). It suffices to consider solutions of the form $\theta_1(s,t) = \tilde{\theta}(s)\mathrm{e}^{\mathrm{i}t}$, with the imaginary part understood to have been taken. The spatial variation of the filament deformation is then given by

$$\tilde{\theta}_1(s) = c_0 \mathrm{e}^{S_{\mathrm{p1}}^2 s} + \mathrm{d}_0 \mathrm{e}^{-S_{\mathrm{p1}}^2 s} + O\left(\frac{1}{M_n^{1/2}}\right). \tag{4.7}$$

On assembling prefactors, we find that, instead of the bending wave being propagated by elastic stresses a distance $\ell_{\mathrm{p}} \sim \Omega^{-1/4} L$ along the filament, magnetic torques carry the wave a potentially much greater distance

$$\ell_{\mathrm{m}} \sim \left(\frac{\pi a^2 B_x^2 \chi^2}{6\mu_0 \zeta_\perp \omega (1-\chi/6)(1+\chi/12)}\right)^{1/2}. \tag{4.8}$$

We call ℓ_{m} the *magnetoviscous length*. Elastic stresses are felt only in a highly curved section of filament near the point of attachment to the cell. Within this *inner layer* we may define a scaled coordinate $S_- = M_n^{1/2}(s+1)$, and

$$\tilde{\boldsymbol{\Theta}}_1(S_-) = \left(A_0 + M_n^{-1/2}A_{1/2}\right)S_- + B_0 + M_n^{-1/2}B_{1/2} + \left(C_0 + M_n^{-1/2}C_{1/2}\right)\mathrm{e}^{-S_-}, \tag{4.9}$$

where we follow Hinch (1991) by using capitalization to distinguish between inner and outer layer variables.

At this order, the boundary conditions at the point of cell attachment (3.9) may be written as

$$D_{\mathrm{t}}\left(-\frac{\partial^3\tilde{\boldsymbol{\Theta}}}{\partial S_-^3} + \frac{\partial\tilde{\boldsymbol{\Theta}}}{\partial S_-}\right) = M_n^{-1/2}\left(\mathrm{i}D_{\mathrm{t}}\Omega_1 a_{\mathrm{c}}\tilde{\boldsymbol{\Theta}} - \frac{\partial^2\tilde{\boldsymbol{\Theta}}}{\partial S_-^2} + \tilde{\boldsymbol{\Theta}} - 1\right), \tag{4.10}$$

$$\mathrm{i}D_{\mathrm{r}}\Omega_1\tilde{\boldsymbol{\Theta}} + a_{\mathrm{c}}\left(\frac{\partial^2\tilde{\boldsymbol{\Theta}}}{\partial S_-^2} + 1 - \tilde{\boldsymbol{\Theta}}\right) = M_n^{-1/2}\,\frac{\partial\tilde{\boldsymbol{\Theta}}}{\partial S_-}. \tag{4.11}$$

Solving these equations up to $O(M_n^{-1/2})$ terms in the boundary layer, and $O(1)$ outside, and matching the two expressions allows us to determine all of the constants featuring in the expressions (4.7) and (4.9). From inner and outer solutions, we can construct a uniformly valid expression for the filament deformation

$$\begin{aligned}\tilde{\theta}_1(s) = {} & \frac{1}{\cosh\left(2\upsilon S_{\mathrm{p1}}^2\right) + \lambda\bar{\upsilon}\sinh\left(2\upsilon S_{\mathrm{p1}}^2\right)}\times\Big[\cosh\left[(s+1)\upsilon S_{\mathrm{p1}}^2\right] + 2\lambda\bar{\upsilon}\sinh\left(\upsilon S_{\mathrm{p1}}^4\right)\\ & \times\cosh\left(s\upsilon S_{\mathrm{p1}}^2\right) + \left(2\frac{a_{\mathrm{c}}i}{D_{\mathrm{r}}S_{\mathrm{p1}}^2}\sinh^2\left(\upsilon S_{\mathrm{p1}}^2\right) - 1 - \lambda\bar{\upsilon}\sinh\left(2\upsilon S_{\mathrm{p1}}^2\right)\right)\mathrm{e}^{-M_n^{1/2}(s+1)}\Big],\end{aligned} \tag{4.12}$$

in which $\lambda \equiv (1/S_{\mathrm{p1}}^2)((a_{\mathrm{c}}^2/D_{\mathrm{r}}) + (1/D_{\mathrm{t}}))$ and $\upsilon \equiv \frac{1}{\sqrt{2}}(1+i)$. We can then read off the time-averaged swimming speed of the micro-swimmer from (3.12)

$$\begin{aligned}\langle \boldsymbol{U}\cdot\boldsymbol{x}\rangle = {} & \frac{b_0^2(\alpha-1)}{4\Omega_1(D_{\mathrm{t}}\alpha+2)K(S_{\mathrm{p1}};\lambda)}\left(\sinh\left(\sqrt{2}S_{\mathrm{p1}}^2\right) - \sin\left(\sqrt{2}S_{\mathrm{p}}^2\right)\right)\\ & \times\left(\sqrt{2}\lambda\left(\cosh\left(\sqrt{2}S_{\mathrm{p1}}^2\right) - \cos\left(\sqrt{2}S_{\mathrm{p1}}^2\right)\right) + \sin\left(\sqrt{2}S_{\mathrm{p1}}^2\right) + \sinh\left(\sqrt{2}S_{\mathrm{p1}}^2\right)\right),\end{aligned} \tag{4.13}$$

where $K(S_{\mathrm{p1}};\lambda) \equiv |\cosh(2\upsilon S_{\mathrm{p1}}^2) + \lambda\bar{\upsilon}\sinh(2\upsilon S_{\mathrm{p1}}^2)|^2$.

For typical values of the cell geometry (3.10), the swimming speed is plotted as a function of the dimensionless frequency $\Omega_1 = S_{\mathrm{p1}}^4$ in figure 5. As the figure makes clear, the asymptotic expression reproduces the dependence of swimming speed upon the dimensionless frequency Ω quite well even at moderate b_0 (in the figure the comparison is made for $b_0 = 1$) for which the *a priori* case for linearizing the governing equations (3.3*a*)–(3.3*d*) is weak.

5. Do magnetic micro-swimmers move like eukaryotic cells?

The magnetic micro-swimmer swims with its filament outstretched before it and propagates a bending wave from the tip to its base, in contrast to many model eukaryotic swimmers, such as sperm cells, which propel themselves with posterior flagella and propagate a bending wave from flagellum base to tip (Brennen & Winet 1977). Tip to basal actuation of anterior flagella is, however, seen in some species of protozoa, among the family Trypanosomatidae (Jahn & Votta 1972) and in the genus *Peranema* (Chen 1950; Chang 1966). Putting such kinematical distinctions aside, in this section we explore a dynamical congruence of the magnetic micro-swimmer to a swimming eukaryotic cell.

The variation of swimming speed with frequency for a typical swimmer is plotted in figure 6 in both dimensionless and dimensional forms. The experimental data are compared with numerical solution of the full equations of motion (3.3*a*)–(3.3*d*) and the asymptotic solution in the limit of large magnetoelastic number (4.13). In addition to the elastic and magnetic properties of the filament, data for the filament length and cell size must be measured from images of the driven filament. A single parameter—the thickness of the lubricating layer supporting the red blood cell, d^*, which feeds into the cell-resistive force coefficients D_t and D_r—cannot be directly measured, and must be determined by fitting the model to the swimming speed data. Fitting the model to the previously published experimental data (Dreyfus *et al.* 2005), we obtain an estimate $d^*=120$ nm, which is consistent with maintenance of the lubrication layer by either the electrostatic forces or the glycocalyx of the red blood cell. Although the magnetoelastic number $M_n=3.42$ of this experimental realization of the magnetic micro-swimmer is not very large, the swimming speed is captured quite well, especially at high frequencies, by the high-M_n asymptotic expression derived in §4*b*; nevertheless the asymptotic result under-predicts the maximum swimming speed and over-predicts the field frequency at which this maximum swimming speed is attained.

With this affirmation of our basic physical picture, we proceed to compare the swimming gait arrived at in the limit $M_n \ll 1$ with a waggled elastic rod, and with the flexible flagellum of a eukaryotic cell. The shape of most of the micro-filament is controlled by a balance of viscous stresses and internal torques $\Omega_1(\partial\theta_1/\partial t) = M_n(\partial^2\theta_1/\partial s)^2$, so that the entire length of the filament is 'active', unlike the waggled rod, in which the propagation of the bending wave is propagated only by elastic stresses and resisted by viscous stresses. The dominant effect of the torque is to apply an effective uniform line tension along the filament, acting to eliminate the difference in orientation of nearby elements. We expect the dominant thrust for propulsion to come from the most highly curved regions of filament near the free and tethered ends. In the limit of large frequencies ($\Omega \gg M_n$), the length scale of these regions, set by the balance of magnetic and viscous torques, is $\ell_\mathrm{m} \sim \Omega_1^{-1/2} L$. Now, our expression (3.17) relating the swimming speed to conformation gives a *dimensional* swimming speed

$$\langle \boldsymbol{U}^* \cdot \hat{\boldsymbol{x}} \rangle \sim \frac{\omega(\alpha-1)}{D_\mathrm{t}\alpha + 2} \langle\langle \theta L^{(1)*} \rangle\rangle, \tag{5.1}$$

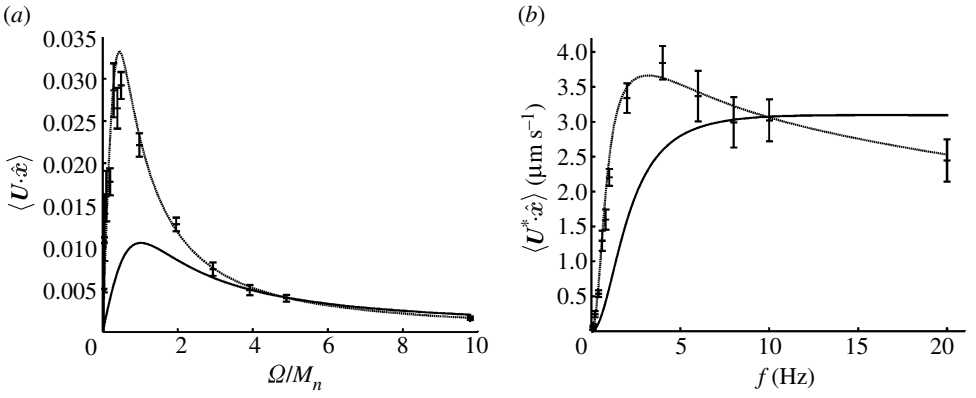

Figure 6. (*a*) Experimentally obtained dimensionless swimming speed against frequency for a cell-tethered swimmer $L=12\,\mu\mathrm{m}$, $B_x=8.9\,\mathrm{mT}$, $B_a=10.3\,\mathrm{mT}$ ($M_n=3.42$; data points). The dashed curve gives the numerical solution of the equations (3.3*a*)–(3.3*d*) and the solid curve gives the asymptotic expression for the swimming speed for large M_n and small b_0 (4.13). (*b*) Unscaled swimming speed data, simulation and asymptotics, in $\mu\mathrm{m\,s}^{-1}$, as a function of frequency.

where $L^{(1)} \sim \int_{-L}^{L} \theta \, \mathrm{d}s^*$ and we use double angled brackets to denote taking both the time and the filament-length average of a quantity; $\langle\langle\cdot\rangle\rangle \equiv \omega/(2\pi L)\int_{-L}^{L}\int_{0}^{2\pi/\omega}\cdot \mathrm{d}t^*\,\mathrm{d}s^*$. Since the maximum angle excursion of the filament (at the free end) is approximately b_0, $\langle\langle\theta L_1\rangle\rangle \sim b_0^2\ell_\mathrm{m}^2/L$, so that

$$\langle \boldsymbol{U}^*\cdot\hat{\boldsymbol{x}}\rangle \sim \left(\frac{K_\mathrm{b}M_n}{L^2}\right)\frac{b_0^2(\alpha-1)}{\zeta_\perp(D_\mathrm{t}\alpha+2)L}, \tag{5.2}$$

where the group $K_\mathrm{b}M_n/L^2$ is independent of both the filament length and the bending stiffness. A more careful analysis (see appendix A*b*) gives us the prefactor 1/4. For a typical magnetic micro-swimmer of length $2L=30\,\mu\mathrm{m}$, field strength 10 mT and frequency $f=20\,\mathrm{Hz}$, the typical torque per unit length applied by the magnetic field is $\tau\approx 10\,\mathrm{pN}$. If the micro-swimmer drags a cell of diameter 6 μm that is supported by a 120 nm thick cushion of fluid, then (5.2) gives a swimming speed estimate $\langle \boldsymbol{U}^*\cdot\hat{\boldsymbol{x}}\rangle \sim 4\,\mu\mathrm{m\,s}^{-1}$, which accords well with the typical swimming speeds obtained in experiment (figure 6*b*).

We compare the swimming speed induced by homogeneous magnetic actuation with the speeds of primitive swimmers sharing this 'bauplan' and limited to the same magnitude of internal torque: a eukaryotic flagellum driven by phased motors exerting torques of amplitude $\sim\tau$, and an elastic rod, where the same total torque $\sim\tau L$ is localized at the end of the filament. The gaits of the three swimmers under the action of these torques are sketched in figure 7.

Various models at all scales of complexity have been proposed for the beating of a flagellum that is driven by metachronously activated dynein motors rather than an applied external field (Machin 1963; Brokaw 1972*a*; Camalet & Jülicher 2000). Consider a cell, with isotropic drag coefficient D_t, propelled by such a flagellum. We follow a minimal treatment of the internal dynamics of the flagellum, assuming that its beating is maintained by some pattern of distributed oscillatory internal torques (Taylor 1952; Machin 1963) with characteristic wavenumber k and uniform amplitude along the flagellum length. Resistance to these torques is supplied by the external viscous drag: recent experiments on

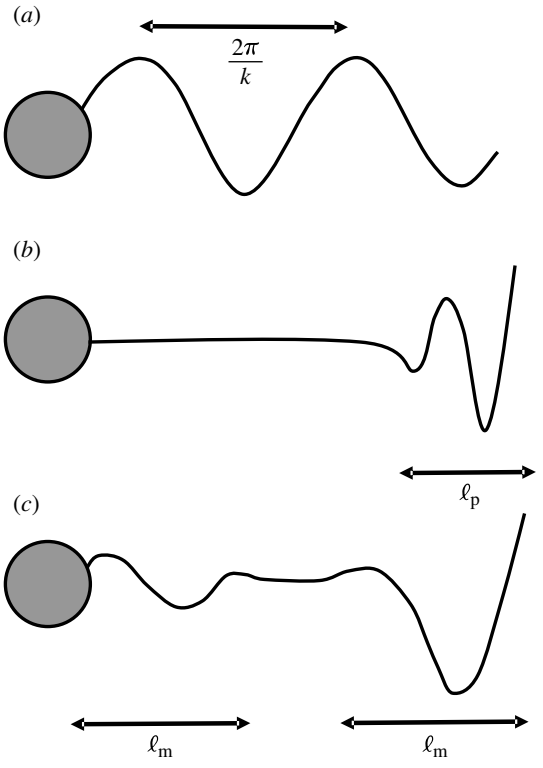

Figure 7. Gaits of three model swimmers subjected to internal torques of the same magnitude $\sim\tau$. (*a*) Eukaryotic cell, with distributed torques and with bending wavelength $2\pi/k$ and amplitude $\sim k\tau/\zeta_\perp\omega$. (*b*) Waggled elastic rod, with total torque τL applied at the free end, with bending wave decay length $\ell_\mathrm{p}\sim(K_\mathrm{b}/\zeta_\perp\omega)^{1/4}$ and amplitude $\sim\tau L/(K_\mathrm{b}\zeta_\perp\omega)^{1/2}$. (*c*) Magnetic micro-swimmer, with bending wave decay length $\ell_\mathrm{m}\sim(\tau/b_0\zeta_\perp\omega)^{1/4}$ and amplitude $\sim b_0\ell_\mathrm{m}$.

pinned and freely swimming bull spermatozoa give an estimate of $\Omega\approx3000$ (Riedel-Kruse *et al.* 2007), showing that the bending stiffness of the flagellum is subdominant. Hence, if we write τ_0 for the amplitude of the internal torque per unit length, then the same balance of viscous and applied torques as control the dynamics of the micro-swimmer will give $\theta\sim k^2\tau_0/\zeta_\perp\omega$ and $L^{(1)*}\sim k\tau_0/\zeta_\perp\omega$ so that the speed of the swimmer can be estimated (again using (3.17)) as

$$\langle\boldsymbol{U}^*\cdot\hat{\boldsymbol{x}}\rangle\sim\frac{\tau_0^2k^3(\alpha-1)}{\zeta_\perp^2\omega(D_\mathrm{t}\alpha+2)}. \tag{5.3}$$

The corresponding scaling of swimming speed with flagellum length depends on whether or not the wavenumber of the bending wave is conserved as the length of the flagellum is increased. Insufficient data exist to distinguish between these two cases. Brennen & Winet (1977) collate data from various flagellated eukaryotic cells, including algae, protozoa and spermatozoa, but unrecorded differences in the flagellum thickness, internal structure and external decoration between these taxa cast doubt upon whether the covariation of bending wavelength with flagellum length can be analysed informatively. Conversely, recent studies of variation in sperm morphological characters between individuals (Birkhead *et al.* 2005) or closely related species (Immler & Birkhead 2007), which could allow

these hidden variables to be controlled for, have not included wavelength data. For this reason, we briefly discuss both possibilities. If k is conserved, so that the filament length is increased by adding additional wavelengths to the filament, then except for the effect of proportionate decrease in head to flagellum drag, which can be neglected if $D_t \ll 1$, flagellum length is a poor predictor of swimming speed (Birkhead *et al.* 2005). If the number of wavelengths is conserved, so that $k \propto 1/L$, then according to (5.3) swimming speed will decrease with the third power of flagellum length, as a result of the lower effectiveness of long-wavelength strokes for locomotion (Taylor 1951).

We can repeat the calculation to determine the swimming speed of the comparable elastic swimmer that would be constructed if the paramagnetic filament were replaced by an elastic filament that is waggled from side to side by an external torque of typical magnitude $\tilde{\tau}_0$ applied at the free end. For such a swimmer, a bending wave will propagate from the free end, with, at high frequencies, a typical damping length $\ell_p \sim (K_b/\zeta_\perp \omega)^{1/4}$ (Wiggins *et al.* 1998). At the waggled end, the rod is bent into an angle $\theta \sim \tilde{\tau}_0 \ell_p / K_b$, so that $L^{(1)*} \sim \tilde{\tau}_0 \ell_p^2 / K_b$ and $\langle\langle \theta L^{(1)*} \rangle\rangle \sim \tau_0^2 \ell_p^4 / K_b^2 L$ and

$$\langle \boldsymbol{U}^* \cdot \hat{\boldsymbol{x}} \rangle \sim \frac{\tilde{\tau}_0^2 (\alpha - 1)}{K_b \zeta_\perp (D_t \alpha + 2) L}. \tag{5.4}$$

The prefactors in this expression have been determined by Lauga (2006).

For a eukaryotic cell of the same dimensions as our typical magnetic micro-swimmer, with $k = 2\pi/L$ (one complete bending wave) and internal torque capped at the value $\tau_0 \sim 10\,\mathrm{pN}$, (5.3) gives an approximate speed $\langle \boldsymbol{U}^* \cdot \hat{\boldsymbol{x}} \rangle \approx 300\,\mu\mathrm{m\,s}^{-1}$, whereas if this same total torque applied to the bending region were all applied at the end of the filament, $\tilde{\tau}_0 \sim \tau_0 \ell_p$, then the swimming speed would be $\langle \boldsymbol{U}^* \cdot \hat{\boldsymbol{x}} \rangle \approx 10\,\mu\mathrm{m\,s}^{-1}$, according to (5.4).

Contrasts with these two primitive cases of flexible swimmer illuminate the swimming dynamics of the magnetic micro-swimmer. Like a eukaryotic flagellum, the shape of the magnetic filament is set by applied torques rather than filament elasticity so that the swimming speed is independent of the elastic modulus K_b. However, just as for the end-actuated elastic swimmer, the propulsive force is generated only near the ends of the magnetic filament, with the bending wave propagating to a distance that is independent of the total filament length. Since the maximum bending angle is in both cases independent of L, the swimming speed decreases like $1/L$ in proportion to the drag acting on the non-propulsive part of the filament. The common independence of swimming speed from actuation frequency of the magnetic micro-swimmer and the waggled elastic rod masks quite stark differences in their swimming gaits. For a magnetic micro-swimmer the maximum angle attained by the filament is independent of driving frequency, and so the distance travelled per stroke declines only with the length over which the bending wave propagates. For a waggled elastic rod the attenuation distance of the bending wave decreases much more slowly with frequency, but is augmented by a decrease in the maximum bending angle. In both cases the decrease in distance travelled per stroke is compensated for exactly by the increased number of stroke cycles.

As we show in appendix A, the scalings of the gait and the swimming speed for the magnetic micro-swimmer exactly reproduce the corresponding waggled rod results once the length scale over which the bending wave propagates ℓ_m decreases below the elastoviscous length ℓ_p, whereupon viscous stresses completely prohibit

rotation of the middle segment of the filament, and a balance of elastic and viscous stresses determines the distance along the filament that the bending wave propagates. Upon entering this regime, the swimming speed starts to decline as $\omega^{-1/2}$, which is to be expected as a special case of (5.4) in which the torque, $\tilde{\tau}_0$, applied at the end of the elastic rod is not allowed to exceed the total magnetic torque, $\tau\ell_{\mathrm{p}}$, acting upon the bending zone of the filament.

6. Designing a fastest swimming micro-swimmer

We draw upon the numerical and asymptotic results of §§4 and 5 in order to determine design principles for building the fastest possible micro-swimmer. Use of such carefully calibrated models allows us to accelerate future experimental optimization of the swimmer. We enjoy control over almost every feature of the micro-swimmer: from the density of the polymer phase present during the assembly of the filament, which controls the stiffness of the tail (Goubault *et al.* 2003), to the size of the cargo. However, the three features of the micro-filament most easily varied in experiment are the filament length, actuation frequency and strength of the applied fields.

We place no constraints upon the efficiency of locomotion, since the energy fed to the swimmer by the applied field is not limited (in contrast, for instance, to spermatozoa, which are believed to operate at the limit of their metabolic output; Cardullo & Baltz 1991). We also focus on the maximization of the *dimensional* swimming speed, $\langle \boldsymbol{U}^{*}\cdot\hat{\boldsymbol{x}}\rangle$, rather than upon the distance travelled by the swimmer in each stroke.

(*a*) *Optimizing in filament length*

We have shown that in the high magnetoelastic number and high-frequency regime, in which most of our experiments are conducted, bending waves initiated at the free and tethered ends of the magnetic filament propagate up to a distance ℓ_{m}, defined in (4.8), inward along the filament. This *magnetoviscous* length plays a role analogous to the elastoviscous length for the optimization of end-actuated elastic swimmers (Wiggins *et al.* 1998). If the filament length $L \gg \ell_{\mathrm{m}}$, then only a fraction of the swimmer will generate useful propulsive force, with the remainder merely contributing to the drag experienced by the swimmer, whereas if $L \ll \ell_{\mathrm{m}}$ then magnetic torques (rather than, as in the case of the waggled elastic rod, the stiffness of the filament) will eliminate all bending in the magnetic filament, leading to a rigid reciprocal stroke and, by Purcell's scallop theorem (Purcell 1977), no net translation of the swimmer from each stroke. We therefore expect the fastest swimming to occur for $L \sim \ell_{\mathrm{m}}$. A more careful calculation using the asymptotic swimming speed (4.13) and taking typical values for the cell geometry (3.10) locates the optimum at $L = 1.19\ell_{\mathrm{m}}$. For a micro-swimmer driven at 20 Hz, with field strength $B_{\mathrm{c}} = 10$ mT, this optimum is realized by a length $2L = 10$ μm, which is slightly shorter than the magnetic filaments that have typically been used.

We remark here that, by freezing the geometrical coefficients representing the tethered end boundary conditions at their values (3.10), it is implicitly assumed that the size of the cargo scales with the length of the magnetic filament. This assumption, which greatly simplifies the analysis, gives only very small

errors for realistic cargo sizes. For the set of cell data used in arriving at the coefficients (3.10), the optimum length predicted in the large M_n, small b_0 limit is shifted only slightly to $L = 0.99\ell_m$: the increased drag associated with the artificial increase in the size of the cargo being partially compensated for by the suppression of the rightward travelling bending wave that starts from the tethered end, and otherwise contributes thrust counter to the swimming direction.

(*b*) *Optimizing in driving frequency*

In §5 we highlighted the insensitivity of the swimming speed to the frequency of actuation. Although the length scale of the propulsive region decreases as frequency increases, the decrease in distance travelled per stroke is compensated for by the increased number of strokes. In appendix A*b* we show that the insensitivity of swimming speed to actuation frequency breaks down once $\Omega \sim M_n^2$, or, equivalently, when the magnetoviscous length (ℓ_m) and elastoviscous length (ℓ_p) become comparable. For a typical swimmer, driven by a field of strength $B_c = 10$ mT, this threshold occurs at a frequency $f \approx 12$ Hz.

(*c*) *Optimizing in field strength*

The dependency of swimming speed upon the strength of the driving fields was shown in figure 3. Variation of the strength of the applied field gives us another method, besides tuning frequency, of altering the magnetoviscous length scale over which bending waves are driven along the actuated filament.

The experimental data of figure 3*a* and simulations of figure 3*b* show swimming speed to increase monotonically with the amplitude of the oscillating field component b_0, a trend that is recapitulated in our various analytical expressions for the swimming speed. The fastest swimming micro-swimmer would therefore be constructed by taking the amplitude of the oscillating field to be as large as experimental constraints permit. There is a limit to how large b_0 can become, however, for if the amplitude of the oscillating field is made too large then the swimmer undergoes a catastrophic 90° change in swimming direction (Gauger & Stark 2006) and starts to swim in the direction of the oscillating component of the field, rather than the steady component.

The torque upon a filament vanishes either if it is aligned with or orthogonal to the external magnetic field. For this reason, filaments in static fields may adopt long-lived folded conformations with sections alternately parallel to and orthogonal to the applied field (Goubault *et al.* 2003; Roper *et al.* 2006). We have exploited such conformations in order to measure the elastic properties of the filament (Goubault *et al.* 2003). We see an analogue of the metastability of field-orthogonal conformations if the swimming filaments are subjected to too large transverse fields: if the frequency of the applied field is large enough that $\ell_m, \ell_p \lesssim L$ so that only a fraction of the filament is bent by the time-varying field, then the time-averaged torque exerted upon the filament vanishes if the length or time-averaged orientation of the filament is aligned with or orthogonal to the steady field component. Both orientations are dynamically permitted, as is shown appendix A*a*. In fact, we will show that, if the mean square oscillatory component is larger than the steady component, then the orthogonal alignment is energetically preferred.

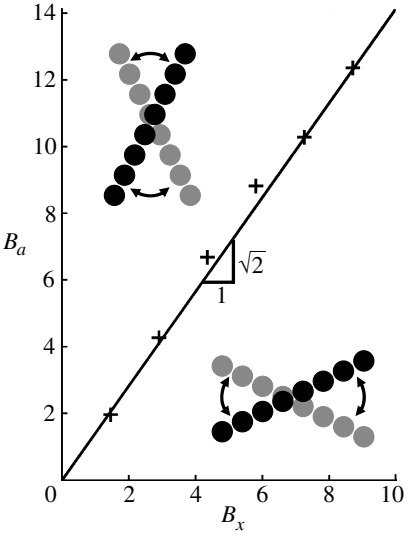

Figure 8. Experimentally observed mean orientation of an ensemble of untethered filaments of different lengths, driven at frequency $f=50$ Hz.

The switch in micro-swimmer orientation from swimming along the steady field component to swimming in the direction of the oscillatory component is most cleanly assayed experimentally for untethered filaments. We build ineffective swimmers—short magnetic filaments that are not tethered to a load—and apply the same configuration of magnetic fields as actuates swimming of a cell-tethered filament. For small amplitude transverse fields, the filament oscillates around a mean orientation $\theta=0$, while for large amplitudes it switches, abruptly, to oscillating around a mean orientation $\theta=\pm\pi/2$. In figure 8, the critical field amplitude at which this switching occurs is plotted when the strengths of the two driving fields are allowed to vary for an ensemble of filaments driven at the same frequency. There is a clear experimental signature that the change occurs when the ratio of field strengths b_0 exceeds $\sqrt{2}$. Below, we support this value with a calculation, valid for micro-swimmers, but which can with very little amendment be applied to untethered filaments as well.

We may explain the critical value at which the swimming direction changes by comparing the total elastic and magnetic energy of the two swimming configurations. This may be done analytically in the case of small M_n, for which the filament shape in the two swimming orientations is already known (appendix A a). When scaled by $K_{\mathrm{b}}L$, the two energy contributions are given by

$$E_{\mathrm{elastic}} = \frac{1}{2}\int_{-1}^{1}\left(\frac{\partial\theta}{\partial s}\right)^2 \mathrm{d}s = \frac{M_n^2}{2}\int_{-1}^{1}\left(\frac{\partial\theta_1}{\partial s}\right)^2 \mathrm{d}s + O(M_n^3), \tag{6.1}$$

$$\begin{aligned} E_{\mathrm{magnetic}} &= -\frac{M_n}{4}\int_{-1}^{1}\left[\left(\frac{2}{\chi}-\frac{1}{12}\right)\left(1+b_0^2\sin^2 t\right)+\left(1-b_0^2\sin^2 t\right)\cos 2\theta\right. \\ &\quad \left.+2b_0\sin t\sin 2\theta\right]\mathrm{d}s \\ &= \frac{M_n}{2}\left(\left(\frac{1}{12}-\frac{2}{\chi}\right)\left(1+b_0^2\sin^2 t\right)\mp\left(1-b_0^2\sin^2 t\right)\right)+4b_0^2M_n^2\int_{-1}^{1}\theta_1\sin t\,\mathrm{d}s, \end{aligned}$$

Table 1. Summary of contrasts between eukaryotic swimmers, elastic rod and magnetic filament.

swimmer	eukaryotic flagellum	elastic rod	magnetic filament (high M_n, $\Omega \sim O(M_n)$)
bending wave propagation	applied (motor)/viscous torques	elastic/viscous torques	applied (magnetic)/ viscous torques
L-dependence	insensitive	sensitive	sensitive
ω-dependence	sensitive	insensitive	insensitive
optimization parameters	frequency and beat form	length	length

plus $O(M_n^3)$ terms, with the positive or negative sign chosen according to whether the filament swims parallel to the steady or oscillatory field components. It follows that the only energy cost paid for swimming in the oscillatory field direction is simply the difference of magnetic energies

$$\Delta E_{\text{magnetic}} = M_n\left(1 - b_0^2 \sin^2 t\right) + O\left(M_n^3\right). \tag{6.2}$$

A micro-swimmer therefore swims in the direction of the oscillatory field component if $b_0 > \sqrt{2}$, and the same threshold value is seen experimentally in figures 3 and 8.

7. Discussion

Magnetically driven micro-swimmers offer the possibility of understanding experimentally the locomotory challenges encountered by eukaryotic cells. We have shown that the dynamics of such swimmers are an admixture of the gaits of a flagellum and of an elastic rod that is waggled from side to side. Bending waves are initiated at both ends of the magnetic tail of the swimmer and, in the physically important case of large magnetoelastic numbers and moderately high frequencies, are propagated by the dual action of viscous and magnetic stresses. This picture gradually breaks down when the very highest frequencies are attained, in which elastic stresses assume a dominant role over magnetic stresses in the transmission of the wave, although not in its initiation. This characterization of the swimming dynamics has allowed us to develop design criteria for optimizing the performance of the magnetic swimmer. The main contrasts in gait and optimization criteria between the three classes of swimmer considered in this article are recapitulated in table 1.

It is interesting to speculate how the swimmer or its environment might be altered to make the swimming kinematics of the magnetic micro-swimmer more closely resemble a eukaryotic cell, and less an end-waggled rod. Firstly, the high-frequency regime in which elastic stresses start to play a dominant role in the propagation of the propulsive bending waves may be postponed if the elastic polymer bridges between particles are allowed to strain-soften. Then as the frequency is increased, and viscous stresses localize bending of the filament near the free end, the increased strain upon the filament (which scales like $\sim b_0 a/\ell_{\text{m}}$, where ℓ_{m} is defined in (4.8)) will cause the elastoviscous length scale to decrease. For sufficiently strong softening ($K_{\text{b}} \sim \epsilon^{-1}$, where ϵ is the strain), the hierarchy of

length scales $\ell_m > \ell_p$ may be maintained indefinitely so that propagation of the bending wave is always driven by the applied torque. Secondly, we can correct the localization of bending itself: for a micro-swimmer immersed in a shear-thinning fluid (specifically with $\eta \sim \omega^{-1}$), the magnetoviscous length can be made independent of ω, so that the magnetic micro-swimmer will use the entire length of its body to propel itself at all frequencies.

The authors would like to thank the Harvard NSEC and the benefactors of the Kao and Kodak fellowships for financial support.

Appendix A. Very high-frequency asymptotics

Design of a fastest swimming micro-swimmer requires tuning of material parameters and of the actuation frequency in order to maximize the dimensional swimming speed $L\omega\langle \boldsymbol{U}\cdot\hat{\boldsymbol{x}}\rangle$. Tuning the actuation frequency to achieve that of the fastest swimming swimmer does not therefore give conditions corresponding to optimization of the *dimensionless* swimming speed which can be seen in figures 4 and 5, but rather to the maximization of the quantity $\Omega\langle \boldsymbol{U}\cdot\hat{\boldsymbol{x}}\rangle$. Optimization of this quantity leads to the selection of frequencies in a higher frequency regime than discussed in §4*a*,*b*, and we extend our asymptotic expressions for the swimming speed into this regime here. By so doing, we find that at very high frequencies the dynamics of the driven magnetic tail of the filament approaches quantitatively the gait of a waggled elastic rod.

(*a*) *Small* M_n

In this high-frequency regime, the dominant balance in the equation of motion (3.3*a*)–(3.3*d*) is between viscous and bending stresses

$$\Omega\frac{\partial\theta_1}{\partial t} = -\frac{\partial^4\theta_1}{\partial s^4}, \tag{A 1}$$

subject to boundary conditions

$$\frac{\partial^2\theta_1}{\partial s^2} + b_0\sin t = 0 \quad \text{and} \quad \frac{\partial\theta_1}{\partial s} = 0 \quad \text{at } s = 1 \tag{A 2}$$

and

$$\left.\begin{aligned} \frac{\partial^2\theta_1}{\partial s^2} + b_0\sin t &= \Omega D_t\left(\frac{\partial^3\theta_1}{\partial s^3} + a_c\frac{\partial\theta_1}{\partial t}\right), \\ D_r\Omega\frac{\partial\theta_1}{\partial t} &= -\left(\frac{\partial^2\theta_1}{\partial s^2} + b_0\sin t\right)a_c + \frac{\partial\theta_1}{\partial s} \quad \text{at} \quad s = -1. \end{aligned}\right\} \tag{A 3}$$

This *hyperdiffusion equation* represents a limit of the well-understood dynamics of flexible, filament-like swimmers (Wiggins *et al.* 1998; Lagomarsino *et al.* 2003; Lauga 2006). Distinct from previous treatments of such swimmers, here the filament is subject to forcing at both ends. This leads to an apparent divergence of the swimming speed if we attempted to apply equation (A 1) down to very small frequencies, since rigid-body motion, which is the usual low-frequency limit of (A 1), cannot simultaneously satisfy both sets of boundary conditions (A 2) and (A 3).

We follow Wiggins *et al.* (1998) by solving (A 1) for the filament shape, by seeking solutions of the form $\theta_1(s,t) = \mathrm{Im}\{\tilde{\theta}_1(s)\mathrm{e}^{\mathrm{i}t}\}$. Such a function will satisfy (A 1) provided that

$$\tilde{\theta}_1(s) = b_0 \sum_{n=1}^{4} A_n \mathrm{e}^{S_\mathrm{p}\alpha_n(1-s)} \quad \text{where} \quad \alpha_n = \exp\left[\frac{\mathrm{i}(n-1)\pi}{2} + \frac{3\pi\mathrm{i}}{8}\right], \tag{A 4}$$

for some set of constants $\{A_n\}$. We have followed previous authors in defining a dimensionless wavenumber $S_\mathrm{p} \equiv \Omega^{1/4}$ (Lagomarsino *et al.* 2003). The boundary conditions (A 2) and (A 3) may then be written as a system of linear equations

$$\mathcal{A}\begin{pmatrix} A_1 \\ A_2 \\ A_3 \\ A_4 \end{pmatrix} = \begin{pmatrix} -1/S_\mathrm{p}^2 \\ 0 \\ -1 \\ -a_\mathrm{c} \end{pmatrix}, \tag{A 5}$$

where the components of the 4×4 matrix $\mathcal{A}$ are

$$\left.\begin{aligned} &\mathcal{A}_{1n} = \alpha_n^2 \quad \mathcal{A}_{2n} = \alpha_n \quad \mathcal{A}_{3n} = \left(\alpha_n^2 S_\mathrm{p}^2 + D_\mathrm{t} S_\mathrm{p}^3 \alpha_n^3 - \mathrm{i}a_\mathrm{c} D_\mathrm{t} S_\mathrm{p}^4\right)\mathrm{e}^{2S_\mathrm{p}\alpha_n}, \\ &\text{and} \\ &\mathcal{A}_{4n} = \left(\mathrm{i}S_\mathrm{p}^4 D_\mathrm{r} + a_\mathrm{c}\alpha_n^2 S_\mathrm{p}^2 + \alpha_n S_\mathrm{p}\right)\mathrm{e}^{2S_\mathrm{p}\alpha_n}. \end{aligned}\right\} \tag{A 6}$$

The coefficients $\{A_n\}$ may be determined on inversion of the matrix $\mathcal{A}$, although their closed-form expressions are too complicated to be reproduced here.

Substituting in (3.11) we then obtain an expression for the time-averaged swimming speed

$$\begin{aligned} \langle \boldsymbol{U}\cdot\hat{\boldsymbol{x}}\rangle = &\frac{M_n^2(\alpha-1)b_0^2}{2(D_\mathrm{t}\alpha+2)}\mathrm{Im}\left\{\sum_{n,m}\frac{A_n\bar{A}_m}{\alpha_n S_\mathrm{p}}\left(\frac{1}{\bar{\alpha}_m S_\mathrm{p}}\mathrm{e}^{2S_\mathrm{p}\bar{\alpha}_m} - \frac{1}{(\alpha_n+\bar{\alpha}_m)S_\mathrm{p}}\right.\right. \\ &\times\left(\exp(2S_\mathrm{p}(\alpha_n+\bar{\alpha}_m))-1\right) - \frac{1}{(D_\mathrm{t}+2)\bar{\alpha}_m^2 S_\mathrm{p}^2}\left(\mathrm{e}^{2\alpha_n S_\mathrm{p}}-1\right)\left(\mathrm{e}^{2S_\mathrm{p}\bar{\alpha}_m}-1\right) \\ &\left.\left.+\frac{a_c}{D_\mathrm{t}+2}\left(\mathrm{e}^{2\alpha_n S_\mathrm{p}}-1\right)\mathrm{e}^{2\bar{\alpha}_m S_\mathrm{p}}\right)\right\}. \end{aligned} \tag{A 7}$$

From this expression and the small M_n asymptotics, we can extract the swimming speed in two important limits, as follows.

(i) In the case $M_n \ll \Omega \ll 1$, we may replace $(1+b_0^2\sin^2 t)\sin(2(\phi-\psi_0))$ by $2b_0\sin t$ in equation (4.5) and then integrate up for ψ_0. Substitution into (3.20) then gives

$$\begin{aligned} \langle \boldsymbol{U}\cdot\hat{\boldsymbol{x}}\rangle \sim &\frac{2(\alpha-1)M_n^2 b_0^2}{5\alpha(D_\mathrm{t}+2/\alpha)(4+D_\mathrm{t}(8+12a_\mathrm{c}+6a_\mathrm{c}^2+3D_\mathrm{r})+6D_\mathrm{r})^2\Omega}\cdot \\ &\times\left[60D_\mathrm{r}+\left(24+80a_\mathrm{c}+60a_\mathrm{c}^2+30D_\mathrm{r}(3+a_\mathrm{c})\right)D_\mathrm{t}\right. \\ &\left.+\left(24+82a_\mathrm{c}+90a_\mathrm{c}^2+30a_\mathrm{c}^3+30D_\mathrm{r}+15a_\mathrm{c}D_\mathrm{r}\right)D_\mathrm{t}^2\right] \end{aligned} \tag{A 8}$$

(ii) In the case $\Omega \gg 1$, the system of linear equations (A 5) can be easily inverted

$$\left.\begin{aligned} A_1 \mathrm{e}^{2\alpha_1} &= \frac{1}{(\alpha_4^2-\alpha_1^2)S_\mathrm{p}^2}, \quad A_2 = \frac{1}{\alpha_2(\alpha_3-\alpha_2)S_\mathrm{p}^2}, \\ A_3 &= \frac{1}{\alpha_3(\alpha_2-\alpha_3)} \quad \text{and} \quad A_4 \mathrm{e}^{2\alpha_4} = \frac{1}{(\alpha_1^2-\alpha_4^2)S_\mathrm{p}^2}, \end{aligned}\right\} \tag{A 9}$$

up to terms of $O(1/S_\mathrm{p}^4)$, on entering which into (A 7) gives

$$\langle \boldsymbol{U}\cdot\hat{\boldsymbol{x}}\rangle \sim \frac{(1+\sqrt{2})(\alpha-1)M_n^2 b_0^2}{4(D_\mathrm{t}\alpha+2)\Omega^{3/2}}. \tag{A 10}$$

(*b*) *Large* M_n

Here the physical picture of §4*b* starts to break down when $\Omega \sim O(M_n^2)$, so that we may write $\Omega = M_n^2\Omega_2$. In this limit, which is easily accessed, if the parameter space is explored by varying the dimensional length of the filament, the dominant influence of viscous stresses extends even into the highly curved regions near the ends of the filament. Analysing (4.6) in this limit, we find an expression for the $O(1)$ shape of the filament that is most easily expressed in stretched coordinates

$$\tilde{\theta}_1(s) = \frac{m_-}{m_-^3-m_+^3}\mathrm{e}^{-m_+S_+} + \frac{m_+}{m_+^3-m_-^3}\mathrm{e}^{-m_-S_+}, \tag{A 11}$$

in which the exponents $m_\pm$ fall out from the auxiliary equation $m_\pm^2 = (1/2)(1\pm\sqrt{1-4\mathrm{i}\Omega_2})$, and we define branches for the square root so that $\mathrm{Re}\{m_\pm\}>0$. Substituting in the expression (3.17) relating swimming speed to filament conformation, we obtain

$$\langle \boldsymbol{U}\cdot\hat{\boldsymbol{x}}\rangle = \frac{\mathrm{i}b_0^2(\alpha-1)}{M_n(D_\mathrm{t}\alpha+2)|m_+^3-m_-^3|^2}\left(\frac{m_-\bar{m}_+(m_+-\bar{m}_-)}{\bar{m}_-m_+(m_++\bar{m}_-)} - \frac{|m_+|^2}{2\bar{m}_-\mathrm{Re}\{m_-\}} - \frac{|m_-|^2}{2\bar{m}_+\mathrm{Re}\{m_+\}}\right), \tag{A 12}$$

where the real part is understood to be taken. Just as for the small M_n, it is not difficult to obtain the low- and high-frequency limits of this expression

(i) for $M_n \ll \Omega \ll M_n^2$: $\langle \boldsymbol{U}\cdot\hat{\boldsymbol{x}}\rangle \sim \frac{M_n b_0^2(\alpha-1)}{4(D_\mathrm{t}\alpha+2)\Omega}$ and

(ii) for $\Omega \gg M_n^2$: $\langle \boldsymbol{U}\cdot\hat{\boldsymbol{x}}\rangle \sim \frac{M_n^2 b_0^2(\alpha-1)}{2\sqrt{2}(D_\mathrm{t}\alpha+2)\Omega^{3/2}}$.

References

Berg, H. & Anderson, R. A. 1971 Bacteria swim by rotating their flagellar filaments. *Nature* **245**, 380–382. (doi:10.1038/245380a0)

Birkhead, T., Pellatt, E., Brekke, P., Yeates, R. & Castillo-Juarez, H. 2005 Genetic effects on sperm design in the zebra finch. *Nature* **434**, 383–387. (doi:10.1038/nature03374)

Brennen, C. & Winet, H. 1977 Fluid mechanics of propulsion by cilia and flagella. *Annu. Rev. Fluid Mech.* **9**, 339–398. (doi:10.1146/annurev.fl.09.010177.002011)

Brokaw, C. J. 1972*a* Computer simulation of flagellar movement. I. Demonstration of stable bend propagation and bend initiation by the sliding filament model. *Biophys. J.* **12**, 564–586.

Brokaw, C. J. 1972*b* Flagellar movement: a sliding filament model. *Science* **178**, 455–462. (doi:10.1126/science.178.4060.455)

Camalet, S. & Jülicher, F. 2000 Generic aspects of axonemal beating. *New J. Phys.* **2**, 24.1–24.23. (doi:10.1088/1367-2630/2/1/324)

Cardullo, R. A. & Baltz, J. M. 1991 Metabolic regulation in mammalian sperm: mitochondrial volume determines sperm length and flagellar beat frequency. *Cell Motil. Cytoskel.* **19**, 180–188. (doi:10.1002/cm.970190306)

Cēbers, A. 2003 Dynamics of a chain of magnetic particles connected with elastic linkers. *J. Phys. Condens. Matter* **15**, S1335–S1344. (doi:10.1088/0953-8984/15/15/303)

Cēbers, A. 2005 Flexible magnetic swimmer. *Magnetohydrodynamics* **41**, 63–72.

Chang, S. 1966 Observations on the organelles, movement, and feeding of peranema trichophorum (Ehrb.) Stein. *Trans. Am. Microsc. Soc.* **85**, 29–45. (doi:10.2307/3224773)

Chattopadhyay, S., Moldovan, R., Yeung, C. & Wu, X. L. 2006 Swimming efficiency of bacterium *Escherichia coli*. *Proc. Natl Acad. Sci. USA* **103**, 13 712–13 717. (doi:10.1073/pnas.0602043103)

Chen, Y. 1950 Investigations of the biology of *Peranema trichophorum* (Euglenineae). *Q. J. Microsc. Sci.* **91**, 279–308.

Cox, R. G. 1970 The motion of long slender bodies in a viscous fluid. Part 1. General theory. *J. Fluid Mech.* **44**, 791–810. (doi:10.1017/S002211207000215X)

Dreyfus, R., Baudry, J., Roper, M. L., Fermigier, M., Stone, H. A. & Bibette, J. 2005 Microscopic artificial swimmers. *Nature* **437**, 862–865. (doi:10.1038/nature04090)

Gauger, E. & Stark, H. 2006 Numerical study of a microscopic artificial swimmer. *Phys. Rev. E* **74**, 021907. (doi:10.1103/PhysRevE.74.021907)

Goubault, C., Jop, P., Fermigier, M., Baudry, J., Bertrand, E. & Bibette, J. 2003 Flexible magnetic filaments as micromechanical sensors. *Phys. Rev. Lett.* **91**, 260802. (doi:10.1103/PhysRevLett.91.260802)

Happel, J. & Brenner, H. 1973 *Low Reynolds number hydrodynamics*, 2nd edn. The Hague, The Netherlands: Martinus Nijhoff Publishers.

Hinch, E. 1991 *Perturbation methods*. Cambridge, UK: Cambridge University Press.

Immler, S. & Birkhead, T. 2007 Sperm competition and sperm midpiece size: no consistent pattern in passerine birds. *Proc. R. Soc. B* **274**, 561–568. (doi:10.1098/rspb.2006.3752)

Jahn, T. & Votta, J. 1972 Locomotion of protozoa. *Annu. Rev. Fluid Mech.* **4**, 93–116. (doi:10.1146/annurev.fl.04.010172.000521)

Koenig, A., Hébraud, P., Gosse, C., Dreyfus, R., Baudry, J., Bertrand, E. & Bibette, J. 2005 Magnetic force probe for nanoscale biomolecules. *Phys. Rev. Lett.* **95**, 128301. (doi:10.1103/PhysRevLett.95.128301)

Lagomarsino, M., Capuani, F. & Lowe, C. 2003 A simulation study of the dynamics of a driven filament in an Aristotelian fluid. *J. Theor. Biol.* **224**, 215–224. (doi:10.1016/S0022-5193(03)00159-0)

Lauga, E. 2006 Floppy swimming: viscous locomotion of actuated elastica. *Phys. Rev. E* **75**, 041916. (doi:10.1103/PhysRevE.75.041916)

Lighthill, J. 1976 Flagellar hydrodynamics: the John von Neumann lecture 1975. *SIAM Rev.* **18**, 161–230. (doi:10.1137/1018040)

Machin, K. E. 1963 The control and synchronization of flagellar movement. *Proc. R. Soc. B* **158**, 88–104. (doi:10.1098/rspb.1963.0036)

Meunier, A. 1994 Friction coefficient of rod-like chains of spheres at very low Reynolds numbers. II. Numerical simulations. *J. Phys. II France* **4**, 561–566. (doi:10.1051/jp2:1994141)

Purcell, E. M. 1977 Life at low Reynolds numbers. *Am. J. Phys.* **45**, 3–11. (doi:10.1119/1.10903)

Purcell, E. M. 1997 The efficiency of propulsion by a rotating flagellum. *Proc. Natl Acad. Sci. USA* **94**, 11 307–11 311. (doi:10.1073/pnas.94.21.11307)

Riedel-Kruse, I. H., Hilfinger, A., Howard, J. & Jülicher, F. 2007 How molecular motors shape the flagellar beat? *HFSP J.* **1**, 192–208. (doi:10.2976/1.2773861)

Roper, M., Dreyfus, R., Baudry, J., Fermigier, M., Bibette, J. & Stone, H. A. 2006 On the dynamics of magnetically driven elastic filaments. *J. Fluid Mech.* **554**, 167–190. (doi:10.1017/S0022112006009049)

Stone, H. A. & Samuel, A. D. T. 1996 Propulsion of microorganisms by surface distortions. *Phys. Rev. Lett.* **77**, 4102–4104. (doi:10.1103/PhysRevLett.77.4102)

Taylor, G. I. 1951 Analysis of the swimming of microscopic organisms. *Proc. R. Soc. A* **209**, 447–461. (doi:10.1098/rspa.1951.0218)

Taylor, G. I. 1952 The action of waving cylindrical tails in propelling microscopic organisms. *Proc. R. Soc. A* **211**, 225–239. (doi:10.1098/rspa.1952.0035)

Wiggins, C. H., Riveline, D., Ott, A. & Goldstein, R. E. 1998 Trapping and wiggling: elastohydrodynamics of driven microfilaments. *Biophys. J.* **74**, 1043–1060.

Yariv, E. 2006 Self-propulsion in a viscous fluid: arbitrary surface deformations. *J. Fluid Mech.* **550**, 139–148. (doi:10.1017/S002211200500830X)

Yu, T. S., Lauga, E. & Hosoi, A. E. 2006 Experimental investigations of elastic tail propulsion at low Reynolds number. *Phys. Fluids* **18**, 091701. (doi:10.1063/1.2349585)